

# First-principles investigation of equilibrium K isotope fractionation among K-bearing minerals

Yonghui Li <sup>a,1</sup>, Wenzhong Wang <sup>a,1</sup>, Zhongqing Wu <sup>a,b,\*</sup>, Shichun Huang <sup>c</sup>

<sup>a</sup> *Laboratory of Seismology and Physics of Earth's Interior, School of Earth and Space, University of Science and Technology of China, Hefei, Anhui 230026, China*

<sup>b</sup> *CAS Center for Excellence in Comparative Planetology, China*

<sup>c</sup> *Department of Geoscience, University of Nevada, Las Vegas, NV 89154, United States*

Received 14 January 2019; accepted in revised form 22 July 2019; Available online 6 August 2019

## Abstract

The  $^{41}\text{K}/^{39}\text{K}$  reduced partition function ratios,  $10^3\ln\beta$ , of 17 major K-bearing minerals have been calculated using the density functional theory (DFT) method. Their  $10^3\ln\beta$  decrease in the order of alunite ( $\text{KAl}_3(\text{SO}_4)_2(\text{OH})_6$ )  $\sim$  K-hollandite I ( $\text{KAlSi}_3\text{O}_8$ )  $>$  niter ( $\text{KNO}_3$ )  $>$  potassium carbonate ( $\text{K}_2\text{CO}_3$ )  $\sim$  potassium bicarbonate ( $\text{KHCO}_3$ )  $>$  muscovite ( $\text{KAl}_2(\text{AlSi}_3\text{O}_{10})(\text{OH})_2$ )  $>$  potassium hydroxide monohydrate ( $\text{KOH}\cdot\text{H}_2\text{O}$ )  $\sim$  hydrated potassium carbonate ( $\text{K}_2\text{CO}_3\cdot 1.5\text{H}_2\text{O}$ )  $>$  nepheline ( $\text{Na}_3\text{KAl}_4\text{Si}_4\text{O}_{16}$ )  $>$  potassium hydroxide dihydrate ( $\text{KOH}\cdot 2\text{H}_2\text{O}$ )  $>$  kalsilite ( $\text{KAlSiO}_4$ )  $>$  microcline ( $\text{KAlSi}_3\text{O}_8$ )  $\sim$  phlogopite ( $\text{KMg}_3\text{AlSi}_3\text{O}_{10}(\text{OH})_2$ )  $>$  lepidolite ( $\text{KLi}_2\text{AlSi}_4\text{O}_{10}(\text{OH})_2$ )  $>$  sylvite ( $\text{KCl}$ )  $>$  leucite ( $\text{KAlSi}_2\text{O}_6$ )  $>$  djerfisherite ( $\text{K}_6\text{CuFe}_{24}\text{S}_{26}\text{Cl}$ ). The calculated  $10^3\ln\beta$  varies from 6.80‰ in alunite to 2.08‰ in djerfisherite at 300 K, and from 0.63‰ to 0.19‰ at 1000 K. At 1000 K, there is only small variation ( $<0.12\%$ ) in  $10^3\ln\alpha_{\text{mineral-microcline}}$  of  $^{41}\text{K}/^{39}\text{K}$ , defined as  $10^3\ln\beta_{\text{mineral}} - 10^3\ln\beta_{\text{microcline}}$ , for K-bearing silicate minerals except K-hollandite I, indicating no measurable K isotope fractionation among these end-member K-bearing minerals during high-temperature geochemistry processes. However, the K concentration variation in K-feldspar shows a significant effect, as large as 0.21‰, on the equilibrium K isotope fractionation between K-feldspar and microcline, which cannot be ignored in high-temperature geochemistry processes. Finally, because  $\text{KOH}\cdot\text{H}_2\text{O}$  and  $\text{KOH}\cdot 2\text{H}_2\text{O}$  are enriched in heavy K isotope relative to all calculated silicate minerals except muscovite, we infer that the interaction between water and silicate minerals likely enriches  $^{41}\text{K}$  in the fluid, which probably explains the relatively higher  $^{41}\text{K}/^{39}\text{K}$  in river and sea water relative to silicate minerals.

© 2019 Elsevier Ltd. All rights reserved.

**Keywords:** Equilibrium K isotope fractionation; Ab initio calculations; K-bearing minerals; Crystal structure; Vibrational frequency

## 1. INTRODUCTION

As a major rock-forming element, potassium (K) is an alkali metal and the 8<sup>th</sup> most abundant element in the Earth's crust, making up about 3 wt% of the crust

(Rudnick and Gao, 2003). It appears in many important minerals in the crust, such as feldspars, leucite, muscovite, and phlogopite. The K abundance varies significantly in different rocks, commonly  $<1\%$  in basalts, 2% to  $>6\%$  in granites and carbonatites (Wedepohl, 1978). Since K is incompatible, felsic rocks have higher K content than basaltic rocks (Wedepohl, 1978). Potassium is also essential for life. For example, it is an electrolyte regulating blood pressure and muscle contraction, and it also plays an important role in the functioning of the kidneys and nerves (Ariyasu et al., 1985; Medhurst et al., 2001; Arnold et al., 2017).

\* Corresponding author at: Laboratory of Seismology and Physics of Earth's Interior, School of Earth and Space, University of Science and Technology of China, Hefei, Anhui 230026, China.

E-mail address: [wuzq10@ustc.edu.cn](mailto:wuzq10@ustc.edu.cn) (Z. Wu).

<sup>1</sup> Co-first authors.

Potassium has two stable isotopes,  $^{39}\text{K}$  (93.2581%) and  $^{41}\text{K}$  (6.7302%), and one radioactive isotope,  $^{40}\text{K}$  (0.0117%). Brewer and Kueck (1934) were among the first to study K isotope compositions in natural rocks. Humayun and Clayton (1995) found relatively homogeneous K isotope compositions in Earth, Moon, and differentiated and undifferentiated meteorites at a level of  $\pm 0.5\text{‰}$  ( $2\sigma$ ) for  $\delta^{41}\text{K}$  ( $\delta^{41}\text{K}_{\text{Standard}} = [((^{41}\text{K}/^{39}\text{K})_{\text{Sample}} / (^{41}\text{K}/^{39}\text{K})_{\text{Standard}}) - 1] \times 1000$ ). Recently, the precision of  $\delta^{41}\text{K}$  measurement has improved to  $\pm 0.05\text{‰}$  ( $2\sigma$ ) (e.g., Li et al., 2016; Wang and Jacobsen, 2016a; Hu et al., 2018; Morgan et al., 2018). At this level of precision, significant K isotope fractionation was reported in some geochemical processes, suggesting that K isotopes could be used as a potential geochemical tracer. For instance, Parendo et al. (2017) documented that the  $\delta^{41}\text{K}$  of hydrothermally altered ocean crust is 0.6‰ greater than unaltered oceanic crust. Consequently, they proposed that K isotopes could be possibly used to trace the recycling of oceanic crust into the mantle wedge. Morgan et al. (2018) also found that seawater and marine and lacustrine K-evaporites are enriched in heavy K isotope relative to silicate minerals, and their  $\delta^{41}\text{K}$  variation is up to 0.6‰, indicating potential applications of stable K isotopes in studying fluid-involved processes. Besides, because K is a moderately volatile element with a 50% condensation temperature of 1006 K (Lodders, 2003) in a solar composition gas at  $10^{-4}$  bar, stable K isotopes have been also used to investigate the formation and evolution of planets and planetesimals. Wang and Jacobsen (2016b) for the first time found that the lunar basalts are enriched in  $^{41}\text{K}$  relative to the Earth and chondrites by  $\sim 0.4\text{‰}$ , which was ascribed to the depletion of K during the formation of the Moon. Therefore, in order to better apply K isotope data into geochemical studies, it is critical to understand the equilibrium isotope fractionation factors among minerals.

Compared to the significant K isotope fractionation found in low-temperature processes, terrestrial basalts exhibit limited variations in K isotope compositions. Wang and Jacobsen (2016a) measured the  $\delta^{41}\text{K}$  of three basalts from different geological settings, and they have similar  $\delta^{41}\text{K}$  values of  $-0.479 \pm 0.027\text{‰}$  ( $2\sigma$ ), which they argue to be representative of the Bulk Silicate Earth (BSE), a value that was later confirmed by Tian et al. (2018) ( $-0.459 \pm 0.011\text{‰}$ ,  $2\sigma$ ) using a much larger sample base. Besides, the small variation of  $\delta^{41}\text{K}$  ( $\sim 0.13\text{‰}$ ) measured in andesites, granodiorites, granites, and obsidian (Li et al., 2016; Hu et al., 2018; Chen et al., 2019; Xu et al., 2019) show limited fractionation among higher temperature processes. However, using ab initio calculations, Li et al. (2019) argued that K concentration in feldspars shows a significant effect on the equilibrium K isotope fractionation factor ( $10^3 \ln \alpha$ ). Specifically, the  $10^3 \ln \alpha$  between feldspar with a K/(K + Na) of 1/16 and microcline can be up to 0.21‰ at 1000 K. Consistent with the ab initio calculation result, Chen et al. (2019) found sodium feldspar (NIST-99a) has  $\delta^{41}\text{K} \sim 0.16\text{‰}$  higher than potassium feldspar (FK-N). Equilibrium K isotope fractionation factors among K-bearing minerals are required to understand the K isotope behaviors during the high-temperature geochemical processes.

First-principles calculations based on density functional theory (DFT) with high prediction power (Lejaeghere et al., 2016) have been used widely to calculate the equilibrium isotope fractionation factors for many isotope systems (e.g., Schauble et al., 2004; Griffith et al., 2008; Méheut et al., 2009; Schauble, 2011; Li and Liu, 2011; Kowalski and Jahn, 2011; Kowalski et al., 2013; Huang et al., 2013; Feng et al., 2014; Liu et al., 2018). Here we extend our previous work focusing only on feldspars (Li et al., 2019) to calculate reduced partition functions of a series of K-bearing minerals, including silicate minerals (K-hollandite I, kalsilite, leucite, lepidolite, microcline, muscovite, nepheline, phlogopite), some potassium salts (alunite, djerfisherite, niter, sylvite, potassium carbonate, hydrated potassium carbonate, potassium bicarbonate), and potashes (potassium hydroxide monohydrate and dihydrate). Their reduced partition function ratios vary significantly, implying large equilibrium K isotope fractionations among those K-bearing minerals. This study provides fundamental data for understanding the K isotope variations in natural samples and their applications in geochemistry and cosmochemistry.

## 2. METHODS

### 2.1. Reduced partition function ratio and equilibrium isotope fractionation

According to Bigeleisen and Mayer (1947) and Urey (1947), the reduced partition function ratio  $\beta_A$  of element X in a condensed phase A, which is the equilibrium isotope fractionation of element X between phase A and an ideal gas of X atoms, can be expressed in the harmonic approximation as:

$$\beta_A = \left( \frac{Q_h}{Q_l} \right) = \prod_{i=1}^{3N-3} \left( \frac{u_{ih}}{u_{il}} \frac{e^{-\frac{1}{2}u_{ih}}}{1 - e^{-\frac{1}{2}u_{ih}}} \frac{1 - e^{-\frac{1}{2}u_{il}}}{e^{-\frac{1}{2}u_{il}}} \right) \quad (1)$$

Here, N is the number of atoms in the system, and the subscript  $i$  is the running index of vibrational modes. Parameters  $u_{ih}$  and  $u_{il}$  are defined as:

$$u_i = \frac{\hbar \omega_i}{kT}, \quad (2)$$

where the subscript  $h$  and  $l$  represent heavy and light isotopes, respectively. Parameters  $\hbar$  and  $k$  are the Planck and Boltzmann constants, respectively;  $T$  is the temperature in Kelvin;  $\omega_i$  is the angular velocity (or angular frequency) of the  $i^{\text{th}}$  mode. The equilibrium isotope fractionation of element X between phases A and B, which is defined as  $\alpha_{A-B} = \beta_A/\beta_B$ , can be expressed in per mil (‰) as:

$$\Delta_{A-B} = 10^3 \ln \alpha_{A-B} = 10^3 \ln \frac{\beta_A}{\beta_B} = 10^3 (\ln \beta_A - \ln \beta_B) \quad (3)$$

### 2.2. First-principles calculations

We follow the same approach used in our previous studies (Huang et al., 2013, 2014; Huang et al., 2013; Feng et al., 2014; Wu et al., 2015; Hu et al., 2016; Wang et al., 2017a,b) using Quantum Espresso software package, which is based

on plane-wave basis set, density functional theory and pseudopotentials (Giannozzi et al., 2009). Our previous studies indicated that the local density approximation (LDA) can well predict the equilibrium volumes within 1% for a series of silicate minerals including diopside, majorite, pyrope, orthenstatite, forsterite, wadsleyite, ringwoodite, and bridgmanite (Huang et al., 2013; Wu et al., 2015). Furthermore, although LDA and GGA (generalized gradient approximation) predict the total different  $10^3 \ln \beta$ , the calculated  $10^3 \ln \alpha$  between minerals and olivine for Mg isotope based on LDA (Huang et al. 2013) agree well with those based on GGA (Schauble, 2011). Thus LDA was adopted in this study to describe the exchange-correlation energy (Perdew and Zunger, 1981) with the energy cut-off for plane-waves set at 70 Rydberg.

The pseudopotentials of H, Li, C, N, O, Na, Mg, Al, Si, S, Cl, K, Fe and Cu used in this paper are listed in Table S1. Some initial crystal structures were downloaded from American Mineralogist Crystal Structure Database (AMCSD) (<http://rruff.geo.arizona.edu/AMS/amcsd.php>) (alunite, djerfisherite, K-hollandite I, kalsilite, leucite, lepidolite, microcline, muscovite, nepheline, phlogopite, niter, sylvite, potassium carbonate and hydrated potassium carbonate), and some from Inorganic Crystal Structure Database (ICSD) (<https://icsd.fiz-karlsruhe.de/search/basic.xhtml>) (potassium bicarbonate, potassium hydroxide monohydrate and dehydrate). The variable cell shape molecular dynamics method (Wentzcovitch, 1991) was applied in the structure optimization with force convergence set at  $10^{-4}$  Ry/Bohr and stress convergence at 0.5 Kbar. Different electronic wave-vector ( $k$ ) mesh samples (see Table S2) were set according to the size of the crystal cell (Fig. 1). The K-O(Cl, S) vibration frequencies were calculated using the density-functional perturbation theory (DFPT) with the phonon wave-vector ( $q$ ) mesh listed in Table S2. The LDA+U method with a self-consistent Hubbard  $U$  value 2.53 eV (Cococcioni and Gironcoli, 2005) was used in the optimization and phonon calculations of djerfisherite.

There are several possible occupancy configurations for muscovite due to Si-Al occupation in the symmetrically nonequivalent sites. We calculated all nonequivalent configurations, and used the configuration with the lowest total energy for vibration frequency calculation. The same approach was also used in  $\text{KOH} \cdot 2\text{H}_2\text{O}$  because of the  $\text{OH}^-$  partial occupancy. The unit cell of K-hollandite I with I4/m space group has 26 atoms; however, the disorder Al-Si partial occupancy breaks the tetragonal symmetry. In order to maintain a tetragonal symmetry, we calculated a  $1 \times 1 \times 2$  supercell, which has two layers of  $\text{K}_2\text{Al}_2\text{Si}_6\text{O}_{16}$  along  $c$ -axis, with one layer on top of another but rotated  $90^\circ$  around the  $c$ -axis (Fig. 1).

### 3. RESULTS

#### 3.1. Relaxed crystal structures and average K-O/S/Cl bond length

The relaxed crystal structures of all calculated minerals are shown in Fig. 1. Our calculated cell parameters agree

well with experimental data (Table 1), with the volume differences between our calculations and measurements ranging from  $-3.2\%$  to  $1.8\%$  for most minerals except alunite, djerfisherite and  $\text{KOH} \cdot 2\text{H}_2\text{O}$ . The calculated volumes for these three minerals are  $4.1\%$ ,  $4.6\%$  and  $5.1\%$  smaller than experimental results, respectively. The average volume difference for all our studied minerals is  $-1.9\%$ . This is because our mineral volume calculations were conducted under the static condition, and the volume expansions contributed by zero-point motion and room temperature were not taken into account. Consequently, our calculated volumes are underestimated by  $\sim 2\%$  (Huang et al., 2013, 2014; Wu et al., 2015; Hu et al., 2016; Qian et al., 2018), consistent with the observed difference between our calculation volumes and experimental data.

The calculated vibrational frequencies of alunite, kalsilite, lepidolite, leucite, microcline, muscovite, niter and phlogopite, agree well with the available experimental data (IR or Raman measurements, Fig. 2), with the slope between calculated frequencies and measured frequencies being  $1.001 \pm 0.025$  ( $1\sigma$ ,  $R^2 = 0.9994$ ). These above comparisons demonstrate that the LDA is a good exchange-correlation functional for the predictions of volume, vibrational frequencies, and equilibrium isotope fractionation among minerals (Huang et al., 2013; Feng et al., 2014; Wu et al., 2015; Hu et al., 2016; Wang et al., 2017a,b). Following the error analyses in Méheut et al. (2009), an uncertainty of  $n\%$  in calculated vibrational frequencies would lead to an uncertainty of  $n\%$  at low temperature and  $2n\%$  at high temperature on the calculated reduced partition function ratio. Our calculated vibrational frequencies are nearly the same as experiment measurements (Fig. 2) with  $2.5\%$  uncertainty. Because the relevant (K-isotope sensitive) vibrational frequencies are low relative to  $kT$ , the uncertainties of our calculated  $10^3 \ln \beta$  and  $10^3 \ln \alpha$  are  $5\%$  and  $7\%$ , respectively.

The ionic radii of  $\text{O}^{2-}$  and  $\text{K}^+$  are  $1.26 \text{ \AA}$  and  $1.52 \text{ \AA}$  (Shannon, 1976), respectively. Thus, we set a  $3.00 \text{ \AA}$  cutoff for K-O bonds to determine the K coordination number (CN) and the average K-O bond length in these minerals (Table 2, Fig. 4, Fig. S1). The average K-Cl bond length in sylvite is defined as the shortest distance between  $\text{K}^+$  and  $\text{Cl}^-$ . In djerfisherite crystal, each  $\text{K}^+$  is connected with eight  $\text{S}^{2-}$  and one  $\text{Cl}^-$ , leading to a CN of nine. The average K-S/Cl bond length is defined as the average length of these nine bond lengths. The calculated average K-O/S/Cl bond lengths (Table 2) vary from  $2.777 \text{ \AA}$  in K-hollandite I (K-O) to  $2.972 \text{ \AA}$  in nepheline (K-O), and from  $3.135 \text{ \AA}$  in sylvite (K-Cl) to  $3.317 \text{ \AA}$  in djerfisherite (K-S/Cl). They increase in the order of: K-hollandite I < alunite < muscovite <  $\text{KOH} \cdot \text{H}_2\text{O}$  <  $\text{KHCO}_3 \sim \text{K}_2\text{CO}_3$  < niter < lepidolite < phlogopite  $\sim \text{K}_2\text{CO}_3 \cdot 1.5\text{H}_2\text{O}$  < microcline <  $\text{KOH} \cdot 2\text{H}_2\text{O}$   $\sim$  leucite  $\sim$  kalsilite < nepheline < sylvite < djerfisherite. Some minerals show the “step-wise” distribution of their individual K-O bond length. For example, in K-hollandite I, the four shortest K-O bonds have the same length of  $2.768 \text{ \AA}$ , and the next four shortest K-O bonds have the same length of  $2.823 \text{ \AA}$ , showing a “step-wise” shape in a K-O bond length distribution graph (Fig. S1). This is consistent with the

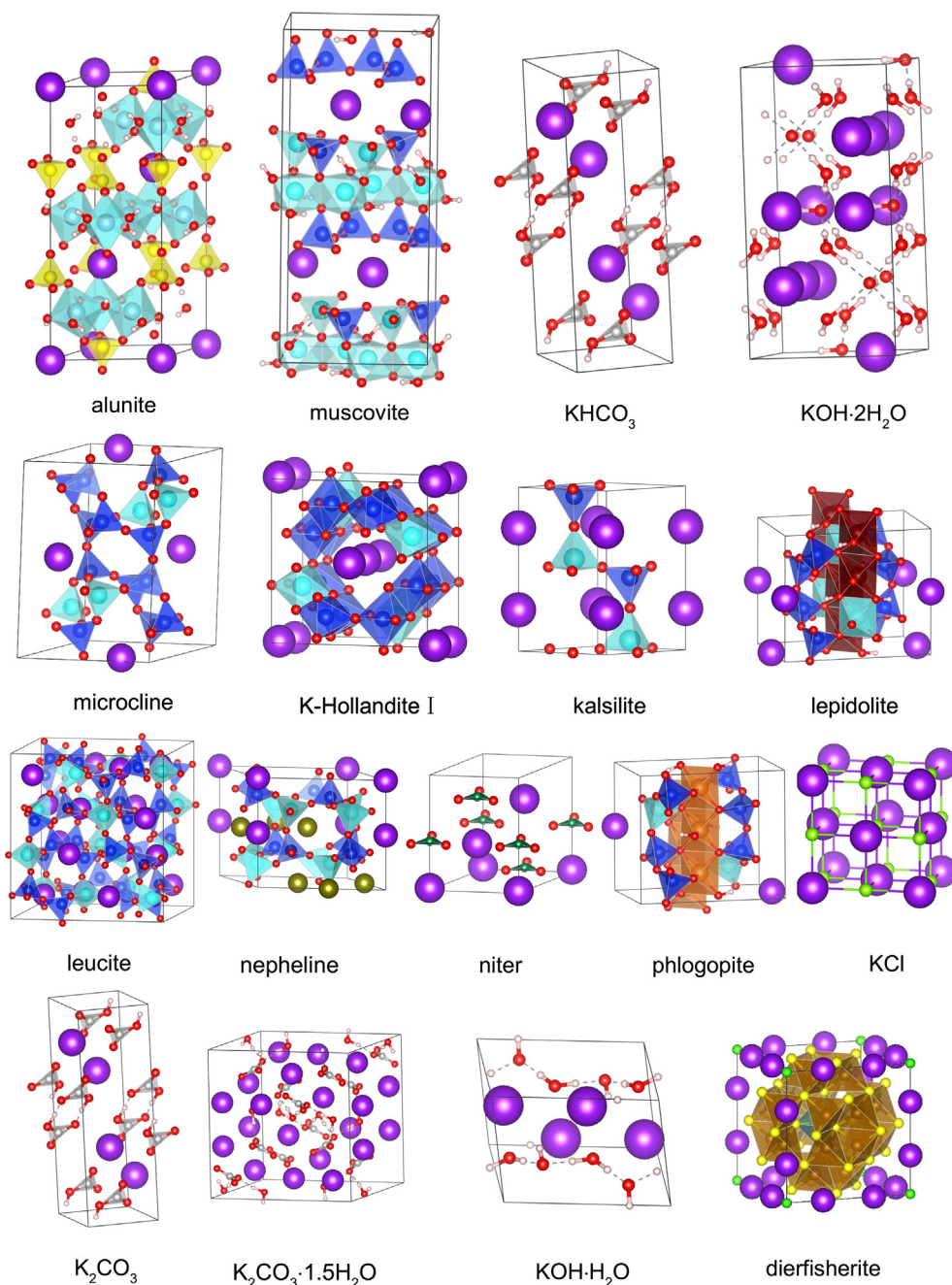


Fig. 1. Crystal structures of minerals calculated in this study: Alunite ( $\text{KAl}_3(\text{SO}_4)_2(\text{OH})_6$ ), djerfisherite ( $\text{K}_6\text{CuFe}_{24}\text{S}_{26}\text{Cl}$ ), K-hollandite I ( $\text{KAlSi}_3\text{O}_8$ ), kalsilite ( $\text{KAlSiO}_4$ ), lepidolite ( $\text{KLi}_2\text{AlSi}_4\text{O}_{10}(\text{OH})_2$ ), leucite ( $\text{KAlSi}_2\text{O}_6$ ), microcline ( $\text{KAlSi}_3\text{O}_8$ ), muscovite ( $\text{KAl}_2(\text{AlSi}_3\text{O}_{10})(\text{OH})_2$ ), nepheline ( $\text{Na}_3\text{KAl}_4\text{Si}_4\text{O}_{16}$ ), niter ( $\text{KNO}_3$ ), phlogopite ( $\text{KMg}_3\text{AlSi}_3\text{O}_{10}(\text{OH})_2$ ), sylvite ( $\text{KCl}$ ), potassium carbonate ( $\text{K}_2\text{CO}_3$ ), potassium bicarbonate ( $\text{KHCO}_3$ ), hydrated potassium carbonate ( $\text{K}_2\text{CO}_3 \cdot 1.5\text{H}_2\text{O}$ ), potassium hydroxide monohydrate ( $\text{KOH} \cdot \text{H}_2\text{O}$ ), and dihydrate ( $\text{KOH} \cdot 2\text{H}_2\text{O}$ ). Colors for atoms: potassium, purple; oxygen, red; silicon, blue; aluminium, cyan; sulfur, yellow; sodium, dark yellow; hydrogen, light pink; magnesium, orange; lithium, brown; nitrogen, olive; chlorine, yellow green; carbon, silver; iron, gold; copper, dark cyan. (For interpretation of the references to colour in this figure legend, the reader is referred to the web version of this article.)

space group of K-hollandite I, which is  $I 4/m$  ( $a = b = 3.42c$ ,  $\alpha = \beta = \gamma = 90^\circ$ ). There are two symmetrically equivalent K atoms and eight O atoms in a unit cell. The K coordinates are K1 (0, 0, 0.5), and K2 (0.5, 0.5, 0). The O coordinates are O1 ( $x$ ,  $y$ , 0), O2 ( $-x$ ,

$-y$ , 0), O3 ( $-y$ ,  $x$ , 0), O4 ( $y$ ,  $-x$ , 0), O5 ( $0.5 + x$ ,  $0.5 + y$ , 0.5), O6 ( $0.5 - x$ ,  $0.5 - y$ , 0.5), O7 ( $0.5 - y$ ,  $0.5 + x$ , 0.5) and O8 ( $0.5 + y$ ,  $0.5 - x$ , 0.5). K1—O1, K1—O2, K1—O3 and K1—O4 bonds have the same length ( $r^2 = a^2x^2 + b^2y^2 + 0.25c^2$ ,  $r$  is the bond length),



Table 1

The relaxed cell parameters of minerals at static conditions compared with X-ray and neutron diffraction data at ambient conditions.

Minerals	a (Å)	b (Å)	c (Å)	$\alpha$ (°)	$\beta$ (°)	$\gamma$ (°)	V (Å <sup>3</sup> )	Volume error (%)	
Alunite	6.894	6.894	16.867			120	694.28	−4.11	This study
	6.974	6.974	17.190			120	724.07		Exp. 1
Djerfisherite	10.222	10.222	10.222				1120.00	−4.62	This study
	10.385	10.385	10.385				1168.22		Exp. 2
K-hollandite I	9.347	9.347	2.714				237.06	0.33	This study
	9.315	9.315	2.723				236.27		Exp. 3
Kalsilite	5.137	5.137	8.726			120	199.45	−1.11	This study
	5.167	5.167	8.725			120	201.69		Exp. 4
Lepidolite	5.138	8.911	10.121		100.22		456.05	−3.14	This study
	5.242	9.055	10.097		100.77		470.83		Exp. 5
Leucite	12.916	12.916	13.776				2298.34	−0.48	This study
	12.931	12.931	13.812				2309.52		Exp. 6
Microcline	8.600	12.943	7.200	90.48	116.30	87.96	717.79	−0.44	This study
	8.571	12.965	7.222	90.64	115.95	87.68	720.99		Exp. 7
Muscovite	5.139	8.897	20.069	89.80	95.73	90.09	912.92	−2.75	This study
	5.199	9.027	20.106		95.78		938.72		Exp. 8
Nepheline	9.997	9.997	8.397			120	726.73	−0.36	This study
	10.01	10.01	8.405			120	729.35		Exp. 9
Niter	5.495	9.356	6.010				308.96	−3.19	This study
	5.414	9.166	6.431				319.14		Exp. 10
Phlogopite	5.259	9.134	10.222		100.10		483.38	−2.04	This study
	5.302	9.180	10.291		99.92		493.45		Exp. 11
Sylvite	6.270	6.270	6.270				246.51	−0.84	This study
	6.288	6.288	6.288				248.61		Exp. 12
K <sub>2</sub> CO <sub>3</sub>	5.721	10.037	6.815		101.18		383.92	1.82	This study
	5.640	9.839	6.874		98.70		377.04		Exp. 13
K <sub>2</sub> CO <sub>3</sub> ·1.5H <sub>2</sub> O	12.080	13.135	7.215		119.71		994.32	0.20	This study
	11.818	13.747	7.109		120.77		992.34		Exp. 14
KHCO <sub>3</sub>	14.656	5.671	3.660		102.22		297.27	−3.20	This study
	15.195	5.630	3.709		104.53		307.11		Exp. 15
KOH·H <sub>2</sub> O	5.838	5.608	7.997		109.92		246.18	−2.94	This study
	5.837	5.851	7.887		109.67		253.64		Exp. 16
KOH·2H <sub>2</sub> O	6.940	6.940	8.372	114.77	114.77	89.38	325.75	−5.11	This study
	7.154	7.154	8.401	115.20	115.20		343.29		Exp. 17

X-ray diffraction: Exp. 1, [Majzlan et al. \(2006\)](#); Exp. 2, [Zaccarini et al. \(2007\)](#); Exp. 3, [Zhang et al. \(1993\)](#); Exp. 4, [Diego et al. \(2010\)](#); Exp. 5, [Guggenheim \(1981\)](#); Exp. 7, [Blasi et al. \(1987\)](#); Exp. 8, [Richardson and Richadson \(1982\)](#); Exp. 9, [Buerger et al., 1954](#); Exp. 10, [Nimmo and Lucas, 1973](#); Exp. 11, [Redhammer and Roth \(2002\)](#); Exp. 12, [Walker et al. \(2004\)](#); Exp. 14, [Skakle et al. \(2001\)](#); Exp. 15, [Allan et al. \(2007\)](#); Exp. 16, [Jacobs et al. \(1984\)](#); Exp. 17, [Rütter and Mootz. \(1991\)](#).

Neutron diffraction: Exp. 6, [Dove et al. \(1993\)](#); Exp. 13, [Idemoto et al. \(1998\)](#).

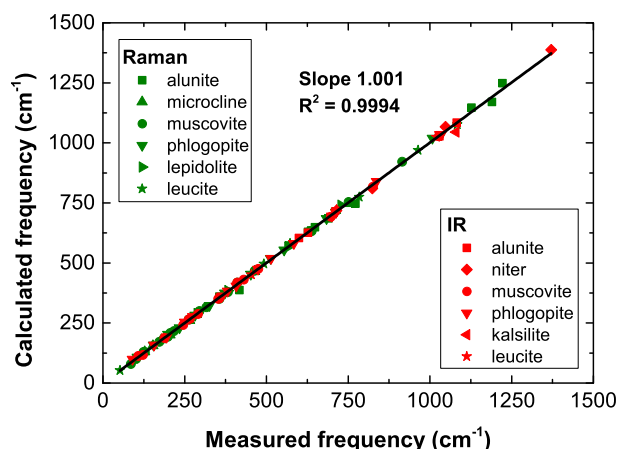


Fig. 2. Calculated vibrational frequencies compared with the available experimental data. Data sources: alunite IR and Raman are from Luo et al. (2009); niter IR and Raman are from Adams and Sharma (1975); microcline IR and Raman are from Li et al. (2017a); muscovite IR, and phlogopite Raman and IR are from Mckeown et al. (1999a,b); kalsilite IR are from Bogdanoviciene et al. (2007); lepidolite Raman are from Li et al. (2017a) and Iordanidis et al. (2014); leucite IR and Raman are from Musić et al. (1997); muscovite Raman are from Mckeown et al. (1999b) and Li et al. (2017a).

and K1—O5, K1—O6, K1—O7 and K1—O8 bonds also have the same length ( $r^2 = a^2(x + 0.5)^2 + b^2(y + 0.5)^2$ ). Thus, the K—O bonds in K-hollandite I have “step-wise” distribution. In contrast, microcline, leucite, three potassium carbonates, and two caustic potashes show gradual increasing distribution graph of K—O bond length, which may result from their lower symmetry.

### 3.2. Reduced partition function ratios

The calculated  $^{41}\text{K}/^{39}\text{K}$  reduced partition function ratios,  $10^3\ln\beta$ , are shown in Fig. 3, and their polynomial fitting parameters are listed in Table 3. Their  $10^3\ln\beta$  decrease in the order of: alunite  $\sim$  K-hollandite I  $>$  niter  $>$   $\text{K}_2\text{CO}_3 \sim \text{KHCO}_3 >$  muscovite  $>$   $\text{KOH}\cdot\text{H}_2\text{O} \sim \text{K}_2\text{CO}_3\cdot 1.5\text{H}_2\text{O} >$  nepheline  $>$   $\text{KOH}\cdot 2\text{H}_2\text{O} >$  kalsilite  $>$  microcline  $\sim$  phlogopite  $>$  lepidolite  $>$  sylvite  $>$  leucite  $>$  djerfisherite. Alunite has the largest  $10^3\ln\beta$  (6.80‰ at 300 K), while djerfisherite has the smallest one (2.08‰ at 300 K). Specially, the equilibrium K isotope fractionation factor ( $10^3\ln\alpha$ ) between  $\text{K}_2\text{CO}_3\cdot 1.5\text{H}_2\text{O}$  and sylvite at 300 K is 0.80‰, which is consistent with that calculated by Li et al. (2017b) (0.67‰ at 300 K) using the generalized gradient approximation (GGA) for the exchange-correlation functional. Using an experimental approach, Li et al. (2017b) reported that at 300 K, the isotope fractionation between  $\text{KHCO}_3$  and  $\text{KHCO}_3$ -saturated solution is near 0.25‰, and that between KCl crystal and KCl-saturated solution is near 0.00‰. Assuming that the  $10^3\ln\beta$  of  $\text{KHCO}_3$ -saturated and KCl-saturated solutions are the same, the K fractionation between  $\text{KHCO}_3$  and KCl is 0.25‰, which is significantly lower than our calculated  $10^3\ln\alpha$  between  $\text{KHCO}_3$  and KCl crystals, 1.18‰ at 300 K. However, these two aqueous solutions ( $\text{KHCO}_3$ -saturated and KCl-saturated solutions) may have different  $10^3\ln\beta$  because of the different  $\text{K}^+$  bonding environments. High KCl content (with KCl of  $\sim 22.8$  wt%,  $\text{K}^+$  of  $\sim 12\%$ ) in KCl-saturated solution suggests that the nearest neighbors of  $\text{K}^+$  in solutions may contain significant amount of  $\text{Cl}^-$  (Varma and Rempe, 2006; Mancinelli et al., 2007; Azam et al., 2009). Since KCl crystal has a lower beta value than  $\text{KHCO}_3$  crystal, we expect that KCl-saturated solution has a lower beta value than  $\text{KHCO}_3$ -saturated solution.

Table 2

The calculated average K—O/S/Cl bond lengths, CN and force constants of K at static conditions.

Minerals	Average K—O/S/Cl bond length (Å)		CN	Force constant of K (N/m)
	Calculated	Experiment		
Alunite	2.803	2.825	12	112.32
Djerfisherite	3.317	3.343	9	34.76
K-hollandite I	2.777	2.733	8	104.65
Kalsilite	2.955	2.975	9	52.50
Lepidolite	2.887	3.022	6	43.59
Leucite	2.931	2.955	6	35.31
Microcline	2.911	2.895	7	48.92
Muscovite	2.826	2.871	6	59.93
Nepheline	2.972	2.992	9	51.90
Niter	2.865	2.876	9	89.51
Phlogopite	2.892	2.961	6	44.85
Sylvite (KCl)	3.135	3.144	6	44.06
$\text{K}_2\text{CO}_3$	2.856	2.832	9	63.82
$\text{K}_2\text{CO}_3\cdot 1.5\text{H}_2\text{O}$	2.895	2.856	8	59.46
$\text{KHCO}_3$	2.850	2.848	8	66.15
$\text{KOH}\cdot\text{H}_2\text{O}$	2.834	2.856	6	57.68
$\text{KOH}\cdot 2\text{H}_2\text{O}$	2.919	2.938	8	53.75

The experiment data from top to bottom are Majzlan et al. (2006); Zaccarini et al. (2007); Zhang et al. (1993); Diego et al. (2010); Guggenheim (1981); Dove et al. (1993); Blasi et al. (1987); Richardson and Richadson (1982); Merlino et al. (1985); Nimmo and Lucas (1973); Redhammer and Roth (2002); Walker et al. (2004); Idemoto et al. (1998); Skakle et al. (2001); Nitta et al. (1952); Jacobs et al. (1984); Rütter and Mootz. (1991).

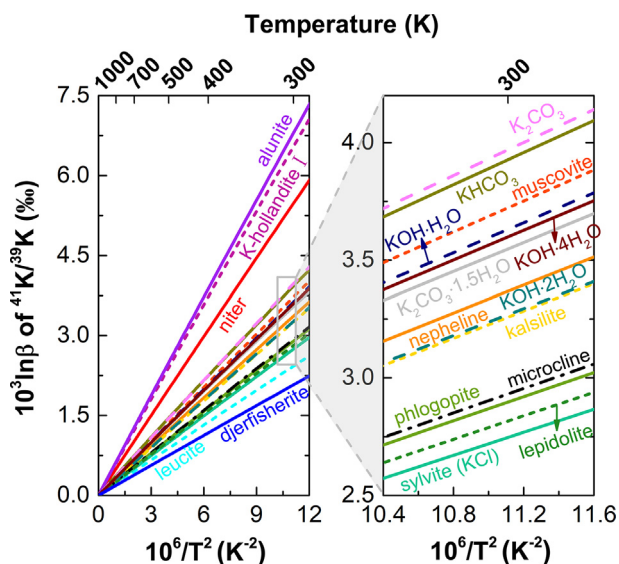


Fig. 3. Temperature-dependent reduced partition function ratio ( $10^3 \ln \beta$ ) of  $^{41}\text{K}/^{39}\text{K}$ .

Table 3

Polynomial fitting parameters of the reduced partition function ratio ( $10^3 \ln \beta$ ) of  $^{41}\text{K}/^{39}\text{K}$ .  $10^3 \ln \beta = Ax + Bx^2 + Cx^3$ , where  $x$  is  $10^6/T^2$ ,  $T$  is the temperature in Kelvin. The temperature range for the polynomial fitting is 270–2000 K.

Minerals	A	B	C
Alunite	0.6304	−1.77E−03	1.24E−05
Djerfisherite	0.1887	−1.77E−04	2.50E−07
K-hollandite I	0.6060	−1.63E−03	1.23E−05
Kalsilite	0.2982	−4.93E−04	4.74E−06
Lepidolite	0.2580	−4.58E−04	4.92E−06
Leucite	0.2221	−3.63E−04	3.65E−06
Microcline	0.2682	−4.38E−04	3.81E−06
Muscovite	0.3419	−6.79E−04	5.41E−06
Nepheline	0.3085	−5.37E−04	4.98E−06
Niter	0.5022	−8.96E−04	6.91E−06
Phlogopite	0.2656	−4.99E−04	4.94E−06
Sylvite	0.2496	−2.23E−04	3.15E−07
$\text{K}_2\text{CO}_3$	0.3643	−7.00E−04	5.65E−06
$\text{K}_2\text{CO}_3 \cdot 1.5\text{H}_2\text{O}$	0.3354	−1.88E−03	3.83E−05
$\text{KHCO}_3$	0.3702	−2.02E−03	4.50E−05
$\text{KOH} \cdot \text{H}_2\text{O}$	0.3375	−1.23E−03	2.30E−05
$\text{KOH} \cdot 2\text{H}_2\text{O}$	0.3024	−9.21E−04	1.68E−05

We also calculated the  $10^3 \ln \beta$  of  $\text{K}_2\text{CO}_3$  and  $\text{K}_2\text{CO}_3 \cdot 1.5\text{H}_2\text{O}$  using GGA to check the effects of different exchange-correlation energy approximations (GGA and LDA) on the  $10^3 \ln \beta$ . The  $10^3 \ln \beta$  between  $\text{K}_2\text{CO}_3$  and  $\text{K}_2\text{CO}_3 \cdot 1.5\text{H}_2\text{O}$  obtained by two approaches are nearly identical (at 300 K, 0.41‰ for GGA and 0.42‰ for LDA). Therefore, the predicted fractionations ( $10^3 \ln \beta$ ) are not noticeably affected by the choice of the exchange-correlation energy approximations.

Among three mica minerals, muscovite has the largest  $10^3 \ln \beta$  while lepidolite has the smallest one (3.72‰ for mus-

covite, 2.90‰ for phlogopite, and 2.82‰ for lepidolite at 300 K). Three K-bearing carbonate minerals ( $\text{K}_2\text{CO}_3$ ,  $\text{KHCO}_3$ , and  $\text{K}_2\text{CO}_3 \cdot 1.5\text{H}_2\text{O}$ ) show a variation of 0.42‰ in  $10^3 \ln \beta$  at 300 K. Potassium carbonate ( $\text{K}_2\text{CO}_3$ ) and bicarbonate ( $\text{KHCO}_3$ ) are enriched in heavy K isotope relative to the hydrous phase  $\text{K}_2\text{CO}_3 \cdot 1.5\text{H}_2\text{O}$ , 3.97‰, 3.93‰ vs 3.55‰ at 300 K. Two caustic potashes hydrates also have slightly different  $10^3 \ln \beta$  values, ranging from 3.63‰ for  $\text{KOH} \cdot \text{H}_2\text{O}$  to 3.27‰ for  $\text{KOH} \cdot 2\text{H}_2\text{O}$  at 300 K. The high-pressure polymorph of K-feldspar, K-hollandite I, has a much larger  $10^3 \ln \beta$  value than its low-pressure phase, microcline, and the difference in their  $10^3 \ln \beta$  is up to 3.62‰ at 300 K and 0.33‰ at 1000 K. In general, the  $10^3 \ln \beta$  of many silicate minerals (kalsilite, microcline, phlogopite, lepidolite, and leucite) are smaller than those of the non-silicate minerals except sylvite and djerfisherite.

## 4. DISCUSSION

### 4.1. Controlling parameters of K isotope equilibrium fractionation

The inter-mineral equilibrium isotope fractionation factor is mainly controlled by their bond strengths and temperature. Stronger bonds correspond to higher vibrational frequencies and, thus, are enriched in heavy isotopes relative to weaker ones (Bigeleisen and Mayer, 1947; Urey, 1947; Schauble et al., 2004; Hill and Schauble, 2008; Young et al., 2009; Wang et al., 2017a,b). Bond strength is affected by many factors, such as bond length, CNs, ionic charge, and the bonded anions. In our previous studies of concentration effects on the  $10^3 \ln \beta$  of Mg, Ca, and K in carbonates, pyroxenes, and feldspars (Feng et al., 2014; Wang et al., 2017a,b; Li et al., 2019), we found that  $10^3 \ln \beta$  of  $^{26}\text{Mg}/^{24}\text{Mg}$  in carbonates,  $^{44}\text{Ca}/^{40}\text{Ca}$  in pyroxenes, and  $^{41}\text{K}/^{39}\text{K}$  in feldspars, are well correlated with their corresponding average Mg—O, Ca—O, and K—O bond lengths, respectively. The bond strengths in these systems are determined by their average bond lengths because other factors such as the CNs and the bonded anions are almost the same. Li et al. (2017b) also found linear correlation between  $\Delta^{41}\text{K}_{\text{mineral-solution}}$  and  $r$  (the average distance between K and its nearest anion) among  $\text{K}_2\text{CO}_3 \cdot 1.5\text{H}_2\text{O}$ ,  $\text{K}_2\text{SO}_4$ ,  $\text{K}_2\text{C}_2\text{O}_4 \cdot \text{H}_2\text{O}$ ,  $\text{K}_2\text{CrO}_4$ , KCl, KBr, and KI.

The relationship between  $10^3 \ln \beta$  of all calculated minerals except sylvite and djerfisherite and their average K—O bond lengths are shown in Fig. 4a. In general, a shorter average bond length corresponds to a larger  $10^3 \ln \beta$  (Fig. 4a).  $10^3 \ln \beta$  is strongly correlated with the average K—O bond length in minerals with the same CNs (Fig. 4a). Specifically, three groups form. Group I is formed by minerals with K CN of 6, and includes muscovite,  $\text{KOH} \cdot \text{H}_2\text{O}$ , phlogopite, lepidolite, and leucite. Group II is formed by minerals with K CN of 8, and includes K-hollandite I,  $\text{KHCO}_3$ ,  $\text{K}_2\text{CO}_3$ ,  $\text{K}_2\text{CO}_3 \cdot 1.5\text{H}_2\text{O}$ , and  $\text{KOH} \cdot 2\text{H}_2\text{O}$ . Group III is formed by minerals with K CN of 9, and includes of niter, kalsilite, and nepheline. At the same average K—O bond length, the mineral with a higher CN has a larger  $10^3 \ln \beta$ . However, there are also some outliers. For example, alunite with a CN of 12 plots on the

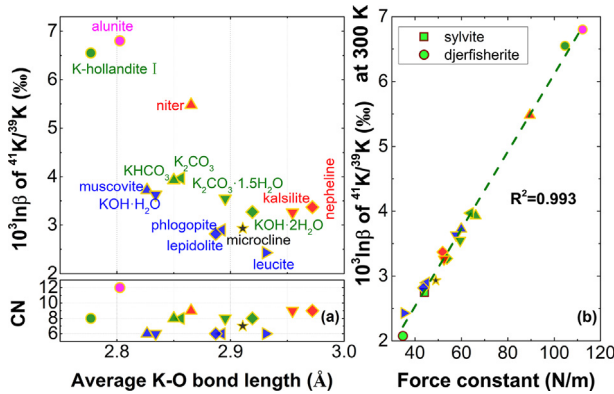


Fig. 4. Reduced partition function ratio ( $10^3 \ln \beta$ ) of  $^{41}\text{K}/^{39}\text{K}$  at 300 K as a function of the calculated average nearest K–O bond length (sylvite and djerfisherite are not included) (a); and force constant (b) of K element in minerals. Minerals with the same CNs painted in the same colors.

trend of Group III. Sylvite (CN = 6) and djerfisherite (CN = 9) are also exceptions. They have much larger bond lengths (3.135 Å and 3.317 Å respectively) and slight smaller  $10^3 \ln \beta$  (2.75‰ and 2.08‰) compared to silicate and carbonate minerals, and they do not plot on any of the trends in Fig. 4a. These exceptions probably reveal that other factors, such as the type of bonded anions and the electronegativities of the first (O anions with K–O bond length small than 3.0 Å) and second (O anions with K–O bond length large than 3.0 Å) nearest-neighbor atoms relative to K, also significantly affect their  $10^3 \ln \beta$  (Méheut and Schauble, 2014).

#### 4.2. Equilibrium K isotope fractionation factors

Because microcline is a common K-bearing mineral in the crust (Anderson and Anderson, 2010), we use microcline as the reference mineral when discussing inter-mineral K stable isotope fractionation factors, defined as  $10^3 \ln \alpha_{\text{mineral-microcline}}$  (Fig. 5, and Table 4). At 1000 K, except for K-hollandite I (0.34‰), all studied silicate minerals have small  $10^3 \ln \alpha_{\text{mineral-microcline}}$ , ranging from 0.07‰ for muscovite to −0.08‰ for leucite (Fig. 5). The small difference of  $10^3 \ln \alpha_{\text{mineral-microcline}}$  among silicate minerals results from their small absolute difference in force constants (=25 N/m), ranging from 59.93 N/m in muscovite to 35.31 N/m in leucite (Fig. 4b and Table 2). Except for K-hollandite I, no obvious K isotope fractionation is expected among most calculated endmember K-bearing silicate minerals during high-temperature geological processes. However, Li et al. (2019) predicted a potentially important concentration effect on  $10^3 \ln \beta$  of feldspars because of large difference in ionic radius between K and Na. Specifically, the equilibrium K isotope fractionation factor between feldspar with a K/(K + Na) of 1/16 and microcline (K/(K + Na) = 1) is 0.21‰ at 1000 K. Therefore, the K concentration effect would probably induce resolvable K isotope fractionation at high temperature (>1000 K). Some K-bearing silicate minerals calculated here are also expected to have concentration effects because

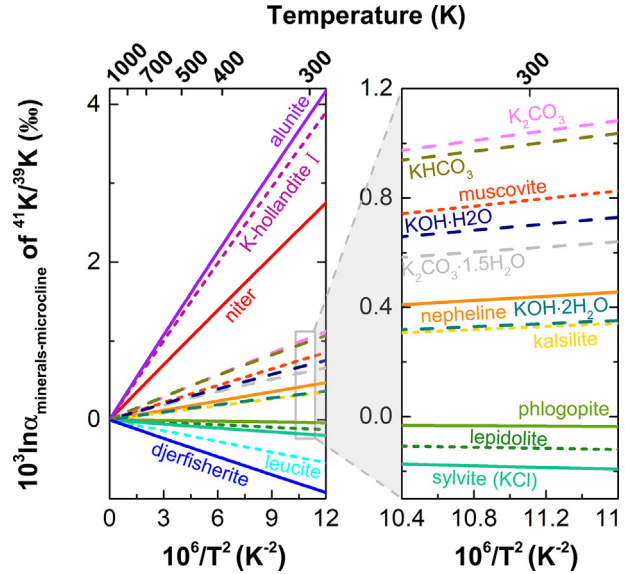


Fig. 5. Equilibrium isotope fractionation  $10^3 \ln \alpha_{\text{minerals-microcline}}$  of  $^{41}\text{K}/^{39}\text{K}$  as a function of  $10^6/T^2$ . Temperature in Kelvin is labeled in the upper of the graph. The right part is the enlarged graph of the dark square region in the left part.

Table 4

Polynomial fitting parameters of the stable fractionation factors ( $10^3 \ln \alpha_{\text{minerals-microcline}}$ ) of  $^{41}\text{K}/^{39}\text{K}$ .  $10^3 \ln \alpha_{\text{minerals-microcline}} = Ax + Bx^2 + Cx^3$ , where  $x$  is  $10^6/T^2$ ,  $T$  is the temperature in Kelvin. The temperature range for the polynomial fitting is 270–2000 K.

Minerals	A	B	C
Alunite	0.3621	−1.33E−03	8.63E−06
Djerfisherite	−0.0785	1.53E−04	−4.13E−07
K-hollandite I	0.3378	−1.19E−03	8.47E−06
Kalsilite	0.0299	−5.44E−05	9.37E−07
Lepidolite	−0.0103	−2.00E−05	1.11E−06
Leucite	−0.0461	7.57E−05	−1.60E−07
Muscovite	0.0737	−2.41E−04	1.61E−06
Nepheline	0.0403	−9.90E−05	1.17E−06
Niter	0.2340	−4.58E−04	3.11E−06
Phlogopite	−0.0026	−6.06E−05	1.14E−06
Sylvite	−0.0186	2.15E−04	−3.49E−06
K <sub>2</sub> CO <sub>3</sub>	0.0961	−2.62E−04	1.84E−06
K <sub>2</sub> CO <sub>3</sub> ·1.5H <sub>2</sub> O	0.0672	−1.44E−03	3.45E−05
KHCO <sub>3</sub>	0.1020	−1.58E−03	4.12E−05
KOH·H <sub>2</sub> O	0.0693	−7.88E−04	1.92E−05
KOH·2H <sub>2</sub> O	0.0664	−7.41E−04	1.58E−05

they typically form solid solutions with Na-endmembers, such as alkali feldspar ((K, Na)AlSi<sub>3</sub>O<sub>8</sub>), nepheline ((K, Na)AlSiO<sub>4</sub>), and hollandite I ((K, Na)AlSi<sub>3</sub>O<sub>8</sub>), a prediction to be tested in future studies. K-hollandite I is the high-pressure phase of K-feldspar from 4 GPa to near 20 GPa (Ferroir et al., 2006; Sueda et al., 2004; Yong et al., 2006). Our calculation (Fig. 5) shows large  $10^3 \ln \beta$  difference between the high and low pressure phases of K-feldspar (K-hollandite I vs. K-spar, 0.34‰ at 1000 K), hinting for possible isotope fractionation during phase transition, similar to Mg and Si isotopes in olivine and its high pressure phases (Wu et al., 2015) (see Table 5).



Table 5

Polynomial fitting parameters of the stable fractionation factors ( $10^3 \ln \alpha_{\text{minerals-KOH} \cdot 2\text{H}_2\text{O}}$ ) of  $^{41}\text{K}/^{39}\text{K}$ .  $10^3 \ln \alpha_{\text{minerals-KOH} \cdot 2\text{H}_2\text{O}} = Ax + Bx^2 + Cx^3$ , where  $x$  is  $10^6/T^2$ ,  $T$  is the temperature in Kelvin. The temperature range for the polynomial fitting is 270–2000 K.

Minerals	A	B	C
Alunite	0.2958	−5.94E−04	−7.21E−06
Djerfisherite	−0.1103	2.98E−04	−9.61E−07
K-hollandite I	0.2715	−4.48E−04	−7.37E−06
Kalsilite	−0.0364	6.86E−04	−1.49E−05
Lepidolite	−0.0766	7.21E−04	−1.47E−05
Leucite	−0.1125	8.17E−04	−1.60E−05
Microcline	−0.0664	7.41E−04	−1.58E−05
Muscovite	0.0074	5.00E−04	−1.42E−05
Nepheline	−0.0261	6.42E−04	−1.47E−05
Niter	0.1677	2.83E−04	−1.27E−05
Phlogopite	−0.0689	6.80E−04	−1.47E−05
Sylvite	−0.0849	9.56E−04	−1.93E−05
$\text{K}_2\text{CO}_3$	0.0298	4.79E−04	−1.40E−05
$\text{K}_2\text{CO}_3 \cdot 1.5\text{H}_2\text{O}$	0.0008	−7.02E−04	1.87E−05
$\text{KHCO}_3$	0.0356	−8.38E−04	2.53E−05
$\text{KOH} \cdot \text{H}_2\text{O}$	0.0030	−4.73E−05	3.36E−06

Significant K isotope fractionation occurs among different K-salts. The  $10^3 \ln \alpha$  between KCl and  $\text{K}_2\text{CO}_3$  is  $-1.22\text{‰}$  at 300 K. Different carbonate and caustic potashes species also significantly affect the enrichment in the heavy K isotope. The  $10^3 \ln \alpha$  among three potassium carbonates and two caustic potashes can be up to  $0.42\text{‰}$  and  $0.70\text{‰}$  at 300 K, respectively. The large equilibrium K isotope fractionations at low temperature predicted by this study imply that K isotopes can be used to investigate K cycles.

#### 4.3. Implications for K isotope geochemistry

In the past several years, high-precision K isotopic measurements of terrestrial basalts, andesites, and granites, show limited  $\delta^{41}\text{K}$  variation, from  $-0.06\text{‰}$  to  $0.02\text{‰}$ , (e.g., Wang and Jacobsen, 2016a,b; Li et al., 2016; Tian et al., 2018; Morgan et al., 2018). In contrast, Morgan et al. (2018) found large  $\delta^{41}\text{K}$  variation ( $>1\text{‰}$ ) in mineral (biotite, feldspars, lepidolite and muscovite) separates from several pegmatites, which was suggested to result from fluid-rock reaction, chemical or thermal diffusion during pegmatite formation. Li et al. (2019) reported important K concentration effect on  $10^3 \ln \beta$  of feldspars using first principles calculations. Specifically, the inter-mineral isotope fractionation factor,  $10^3 \ln \alpha_{\text{feldspar-microcline}}$ , is up to  $0.42\text{‰}$  at 700 K and  $0.21\text{‰}$  at 1000 K for a feldspar with a  $\text{K}/(\text{K} + \text{Na})$  ratio of 0.0625. This effect may contribute to part of the large  $\delta^{41}\text{K}$  variation in pegmatite minerals observed by Morgan et al. (2018); however, they did not report mineral chemical compositions.

Large  $\delta^{41}\text{K}$  variation has been observed in rocks that experienced low temperature processes, such as hydrothermal alteration. Because seawater is significantly enriched in  $^{41}\text{K}$  relative to igneous rocks (Li et al., 2016; Wang and Jacobsen, 2016a; Lee et al., 2018), oceanic crust and seawater interaction would be expected to induce  $\delta^{41}\text{K}$  variations in altered oceanic crust. Parendo et al. (2017) found large

and systemic  $\delta^{41}\text{K}$  variations in altered oceanic crust that are ascribed to hydrothermal alteration. This finding suggests that K isotopes can be used to trace the recycling of oceanic crust into the mantle. Knowledge of K isotope fractionations between silicate minerals and seawater is required to better understand the  $\delta^{41}\text{K}$  characteristics of altered oceanic crust.

Theoretical calculations of  $\text{K}^+ 10^3 \ln \beta$  in aqueous fluids is a challenge, because aqueous solution does not have a regular structure. Li et al. (2017b) measured the K isotope fractionations between K-salts and saturated K solutions. In their experiments, they found both negative (KBr and KI) and positive ( $\text{K}_2\text{CO}_3 \cdot 1.5\text{H}_2\text{O}$ ,  $\text{K}_2\text{SO}_4$ ,  $\text{KHCO}_3$  and  $\text{K}_2\text{C}_2\text{O}_4 \cdot \text{H}_2\text{O}$ ) fractionations between K-salts and aqueous solutions of the same type of salts, while there is no measurable fractionation between sylvite and a KCl-saturated solution ( $0.02 \pm 0.12\text{‰}$ ). However, it seems inappropriate to use a KCl-saturated solution (with KCl of  $\sim 22.8\text{ wt\%}$ ,  $\text{K}^+$  of  $\sim 12\text{‰}$ ) to approximate river and sea water which have  $\text{K}^+$  abundance  $<0.04\text{ wt\%}$  (Livingston, 1963; Millero et al., 2008), because  $\text{K}^+$  bonding environment in KCl-saturated solution is totally different from that in a diluted K aqueous solution (Varma and Rempe, 2006; Azam et al., 2009; Rowley and Roux, 2012). K content in aqueous solution would probably also affect the surrounding environment around  $\text{K}^+$  (Mancinelli et al., 2007).

In diluted aqueous solutions,  $\text{K}^+$  cations are directly linked to  $\text{O}^{2-}$  anions with a CN of 6–8, and the K-O distances range from  $2.5 \text{ \AA}$  to  $3.5 \text{ \AA}$  with a sharp peak of  $g(r)$  (RDF, radial distribution functions) near  $2.83 \text{ \AA}$  (Azam et al., 2009). Potassium hydroxides,  $\text{KOH} \cdot \text{H}_2\text{O}$  and  $\text{KOH} \cdot 2\text{H}_2\text{O}$ , have K-O bond lengths and CNs similar to those of aqueous  $\text{K}^+$  (Table 2, Fig. 4a), implying that the  $\text{K}^+ 10^3 \ln \beta$  of diluted aqueous solution should be close to those of potassium hydroxides. If this is the case, our results demonstrate that all calculated K-bearing silicate

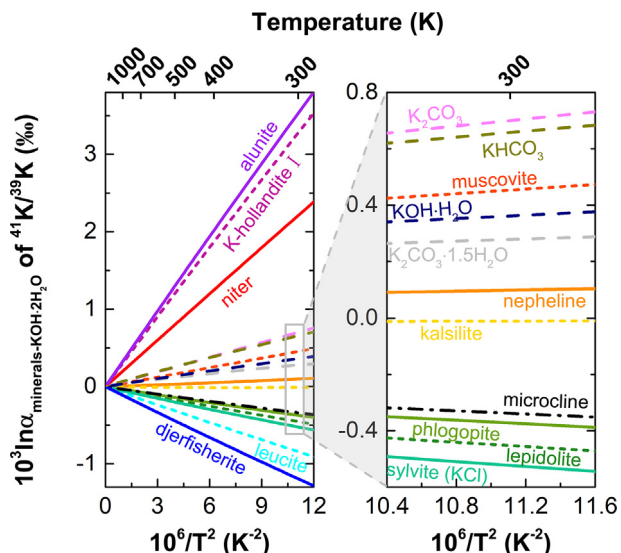


Fig. 6. Equilibrium isotope fractionation  $10^3 \ln \alpha_{\text{minerals-KOH} \cdot 2\text{H}_2\text{O}}$  of  $^{41}\text{K}/^{39}\text{K}$  as a function of  $10^6/T^2$ . Temperature in Kelvin is labeled in the upper of the graph. The right part is the enlarged graph of the dark square region in the left part.

minerals, except for muscovite, are enriched in light K isotopes relative to aqueous solution (seawater) (Fig. 6). For instance, the  $10^3\ln\alpha$  between microcline and aqueous  $K^+$  ranges from  $-0.19$  to  $-0.09\%$  at 600 K. Thus, it is expected that light K isotopes would be preferentially incorporated into residual silicate phases during the water-rock interaction. In addition, it can be also inferred that the fluid probably leaches out heavy K isotopes from silicate rocks during weathering processes, which might explain the observation that river and sea water have higher  $^{41}K/^{39}K$  ratios relative to silicate rocks (Li et al., 2016; Wang and Jacobsen, 2016a; Lee et al., 2018). The quantitative analyses of K isotopic behaviors during low-temperature processes involving fluids require knowledge of equilibrium K isotope fractionations and K isotope exchange rates between minerals and aqueous  $K^+$ , which needs to be determined in future researches.

## 5. CONCLUSIONS

The reduced partition function ratios ( $10^3\ln\beta$ ) of 17 major K-bearing minerals are calculated using the DFT method. The  $10^3\ln\beta$  of  $^{41}K/^{39}K$  decreases in the order of: alunite, K-hollandite I, niter, potassium carbonate, potassium bicarbonate ( $KHCO_3$ ), muscovite, potassium hydroxide monohydrate ( $KOH\cdot H_2O$ ), hydrated potassium carbonate ( $K_2CO_3\cdot 1.5H_2O$ ), potassium hydroxide dihydrate ( $KOH\cdot 2H_2O$ ), nepheline, kalsilite, microcline, phlogopite, lepidolite, sylvite (KCl), leucite, and djerfisherite.

Our results demonstrate that the equilibrium K isotope fractionation among end-member K-bearing silicate minerals is limited at high temperature ( $>1000$  K). This may explain the observation that no resolvable variation in K isotope composition occurs in high temperature igneous processes. However, our previous study (Li et al., 2019) found that K concentration in feldspar shows a significant effect on the equilibrium K isotope fractionation, and the  $10^3\ln\alpha$  between feldspar with low K concentration ( $K/(K + Na) = 1/16$ ) and microcline can be up to  $0.21\%$  at 1000 K. This suggests that resolvable K isotope fractionation among minerals could be produced by the variation of K concentration if the K concentration is extremely low ( $K/(K + Na) < 1/16$ ). Instead, the K concentration effect on the  $10^3\ln\alpha$  is likely unresolvable at high temperature when K concentration is relatively high in silicate minerals.

In contrast, at low temperature, the  $10^3\ln\alpha$  among all calculated minerals becomes obviously large because  $10^3\ln\beta$  and  $10^3\ln\alpha$  are proportional to  $1/T^2$ . For instance,  $10^3\ln\alpha$  between muscovite and microcline could be up to  $0.79\%$  at 300 K.  $KOH\cdot H_2O$  and  $KOH\cdot 2H_2O$  have similar K–O bond lengths and CNs to those of aqueous  $K^+$ , suggesting that the  $10^3\ln\beta$  of aqueous  $K^+$  might be close to those of potassium hydroxides. If the  $10^3\ln\beta$  range for caustic potashes is adopted as the possible  $10^3\ln\beta$  for aqueous  $K^+$ , all calculated K-bearing silicate minerals except muscovite are enriched in light K isotopes relative to aqueous  $K^+$ . Therefore, it is expected that light K isotopes would be preferentially incorporated into residual silicate phases during the water-rock interaction, and that the fluid proba-

bly carries out heavy K isotopes from silicate rocks during weathering processes, leading to heavy K isotopes in river and sea waters.

## ACKNOWLEDGEMENTS

This work is financially supported by the Strategic Priority Research Program (B) of the Chinese Academy of Sciences (grant XDB18000000), Natural Science Foundation of China (41721002), the Fundamental Research Funds for the Central Universities (WK2080000078). The computations were conducted partly in Supercomputing Center of the University of Science and Technology of China. SH was supported by NSF EAR-1524387. We thank three anonymous reviewers, and AE Ed Schauble for their constructive reviews which significantly improve this paper.

## APPENDIX A. SUPPLEMENTARY MATERIAL

Supplementary data to this article can be found online at <https://doi.org/10.1016/j.gca.2019.07.038>.

## REFERENCES

- Adams D. and Sharm S. (1975) Vibrational spectroscopy at very high pressure Part 7. -Ir. Spectra of Potassium Nitrate. *J. Chem. Soc., Faraday Trans. 2*, **72**, 1344–1353.
- Allan D. R., Marshall W. G. and Pulham C. R. (2007) The high-pressure crystal structure of potassium hydrogen carbonate ( $KHCO_3$ ). *Am. Mineral.* **92**, 1018–1025.
- Anderson, R.S., Anderson, S.P., 2010. Geomorphology: The Mechanics and Chemistry of Landscapes. Cambridge University Press, The Edinburgh Building, Cambridge CB2 8RU, UK.
- Ariyasu R. G., Nichol J. A. and Ellisman M. H. (1985) Localization of sodium/potassium adenosine triphosphatase in multiple cell types of the murine nervous system with antibodies raised against the enzyme from kidney. *J. Neurosci.* **5**, 2581–2596.
- Arnold R., Pianta T. J., Pussell B. A., Kirby A., O'Brien K., Sullivan K., Holyday M., Cormack C., Kiernan M. C. and Krishnan A. V. (2017) Randomized, controlled trial of the effect of dietary potassium restriction on nerve function in CKD. *Clin J Am Soc Nephrol.* **12**, 1569–1577.
- Azam S., Hofer T., Randolph B. and Rode B. (2009) Hydration of sodium(I) and potassium(I) revisited: A comparative QM/MM and QMCF MD simulation study of weakly hydrated ions. *J. Phys. Chem. A*, **113**, 1827–1834.
- Bigeleisen J. and Mayer M. G. (1947) Calculation of equilibrium constants for isotopic exchange reactions. *J. Chem. Phys.* **15**, 261.
- Blasi A., Blasi C. D. P. and Zanazzi P. F. (1987) A re-examination of the pellets microcline: mineralogical implications and genetic consideration. *Can. Mineral.* **25**, 527–537.
- Bogdanoviciene I., Jankeviciute A., Pinkas J., Beganskienė A. and Kareiva A. (2007) Sol-gel synthesis and characterization of kalsilite-type aluminosilicates. *Mater. Sci-Medzg.* **13**, 1392–11320.
- Brewer A. K. and Kueck P. D. (1934) The relative abundance of the isotopes of lithium, potassium and rubidium. *Phys. Rev.* **46**, 894–897.
- Buerger M. J., Klein G. E. and Donnay G. (1954) Determination of the crystal structure of nepheline. *Am. Mineral.* **39**, 805–818.
- Chen H., Tian Z., Brenna T.-R., Randy L. K. and Wang K. (2019) High-precision potassium isotopic analysis by MC-ICP-MS: an inter-laboratory comparison and refined K atomic weight. *J. Anal. Atmos. Spectrom.* **34**, 160–171.

- Cococcioni M. and Gironcoli S. (2005) Linear response approach to the calculation of the effective interaction parameters in the LDA+U method. *Phys. Rev. B* **71** 035105.
- Diego Gatta G., Angel R. J. and Carpenter M. A. (2010) Low-temperature behavior of natural kalsilite with P31c symmetry: An in situ single-crystal X-ray diffraction study. *Am. Mineral.* **95**, 1027–1034.
- Dove M. T., Cool T., Palmer D. C., Putnis A., Salje E. K. H. and Winkler B. (1993) On the role of Al-Si ordering in the cubic-tetragonal phase transition of leucite. *Am. Mineral.* **78**, 486–492.
- Feng C., Qin T., Huang S., Wu Z. and Huang F. (2014) First principles investigations of equilibrium calcium isotope fractionation between clinopyroxene and Ca-doped orthopyroxene. *Geochim. Cosmochim. Acta* **143**, 132–142.
- Ferroir T., Onozawa T., Yagi T., Merkel S., Miyajima N. H., Nishiyama N., Irifune T. and Kikegawa T. (2006) Equation of state and phase transition in KAlSi3O8 hollandite at high pressure. *Am. Mineral.* **91**, 327–332.
- Giannozzi P., Baroni S., Bonini N., Calandra M., Car R., Cavazzoni C., Ceresoli D., Chiarotti G. L., Cococcioni M., Dabo I., Dal Corso A., de Gironcoli S., Fabris S., Fratesi G., Gebauer R., Gerstmann U., Gougousis C., Kokalj A., Lazzeri M., Martin-Samos L., Marzari N., Mauri F., Mazzarello R., Paolini S., Pasquarello A., Paulatto L., Sbraccia C., Scandolo S., Sclauzero G., Seitsonen A. P., Smogunov A., Umari P. and Wentzcovitch R. M. (2009) QUANTUM ESPRESSO: a modular and open-source software project for quantum simulations of materials. *J. Phys. Condens. Matter* **21** 395502.
- Griffith E. M., Schauble E. A., Bullen T. D. and Paytan A. (2008) Characterization of calcium isotopes in natural and synthetic barite. *Geochim. Cosmochim. Acta* **72**, 5641–5658.
- Guggenheim S. (1981) Cation ordering in lepidolite. *Am. Mineral.* **66**, 1221–1232.
- Hill P. S. and Schauble E. A. (2008) Modeling the effects of bond environment on equilibrium iron isotope fractionation in ferric aquo-chloro complexes. *Geochim. Cosmochim. Acta* **72**, 1939–1958.
- Hu Y., Wu Z., Dera P. K. and Bina C. R. (2016) Thermodynamic and elastic properties of pyrope at high pressure and high temperature by first-principles calculations. *J. Geophys. Res. Sol. Ea.* **121**, 6462–6476.
- Hu Y., Chen X., Xu Y. and Teng F. (2018) High-precision analysis of potassium isotopes by HR-MC-ICPMS. *Chem. Geol.* **493**, 100–108.
- Huang F., Chen L., Wu Z. and Wang W. (2013) First-principles calculations of equilibrium Mg isotope equilibrium fractionations between garnet, clinopyroxene, orthopyroxene, and olivine: implications for Mg isotope thermometry. *Earth Planet. Sci. Lett.* **367**, 61–70.
- Huang F., Wu Z., Huang S. and Wu F. (2014) First-principles calculations of equilibrium silicon isotope equilibrium fractionation among mantle minerals. *Geochim. Cosmochim. Acta* **140**, 509–520.
- Humayun M. and Clayton R. (1995) Potassium isotope cosmochemistry: Genetic implications of volatile element depletion. *Geochim. Cosmochim. Acta* **59**, 2131–2148.
- Idemoto Y., Richardson J. W., Koura N., Kohara S. and Loong C. K. (1998) Crystal structure of  $(\text{Li}_x\text{K}_{1-x})_2\text{CO}_3$  ( $x = 0, 0.43, 0.5, 0.62, 1$ ) by neutron powder diffraction analysis. *J. Phys. Chem. Solid.* **56**, 363–376.
- Iordanidis A., Garcia-Guinea J., Garas S., Asvesta A. and Triantafyllou A. G. (2014) Application of  $\mu$ Raman microscopy to the identification of individual airborne particles: Preliminary results from Kozani's Area, Northern Greece. *Part. Sci. Technol.* **32**, 355–359.
- Jacobs H., Tacke T. and Kockelkorn J. (1984) Hydroxidmonohydrate des Kaliums und Rubidiums; Verbindungen, deren Atomanordnungen die Schreibweise  $\text{K}(\text{H}_2\text{O})\text{OH}$  bzw.  $\text{Rb}(\text{H}_2\text{O})\text{OH}$  nahelegen. *Z. Anorg. Allg. Chem.* **516**, 67–78.
- Kowalski P. M. and Jahn S. (2011) Prediction of equilibrium Li isotope equilibrium fractionation between minerals and aqueous solutions at high P and T: an efficient ab initio approach. *Geochim. Cosmochim. Acta* **75**, 6112–6123.
- Kowalski P. M., Wunder B. and Jahn S. (2013) Ab initio prediction of equilibrium boron isotope equilibrium fractionation between minerals and aqueous fluids at high P and T. *Geochim. Cosmochim. Acta* **101**, 285–301.
- Lee H. L., Peucker-Ehrenbrink B., Chen H., Hasenmueller E. A. and Wang K. (2018) Potassium isotopes in major world rivers: Implications for weathering and seawater budget. In Goldschmidt Abstracts.
- Lejaeghere K., Bihlmayer G., Bjorkman T., Blaha P., Blugel S., Blum V., Caliste D., Castelli I. E., Clark S. J., Dal Corso A., de Gironcoli S., Deutsch T., Dewhurst J. K., Di Marco I., Draxl C., Duak M., Eriksson O., Flores-Livas J. A., Garrity K. F., Genovese L., Giannozzi P., Giantomassi M., Goedecker S., Gonze X., Granas O., Gross E. K. U., Gulans A., Gygi F., Hamann D. R., Hasnip P. J., Holzwarth N. A. W., Iu an D., Jochym D. B., Jollet F., Jones D., Kresse G., Koepernik K., Kucukbenli E., Kvashnin Y. O., Loch I. L. M., Lubeck S., Marsman M., Marzari N., Nitzsche U., Nordstrom L., Ozaki T., Paulatto L., Pickard C. J., Poelmans W., Probert M. I. J., Refson K., Richter M., Rignanese G. M., Saha S., Scheffler M., Schlipf M., Schwarz K., Sharma S., Tavazza F., Thunstrom P., Tkatchenko A., Torrent M., Vanderbilt D., van Setten M. J., Van Speybroeck V., Wills J. M., Yates J. R., Zhang G. X. and Cottenier S. (2016) Reproducibility in density functional theory calculations of solids. *Science* **351**(6280). <https://doi.org/10.1126/science.aad3000>, aad3000–aad3000.
- Li W., Beard B. and Li S. (2016) Precise measurement of stable potassium isotope ratios using a single focusing collision cell multi-collector ICP-MS. *J. Anal. At. Spectrom.* **31**, 1023–1029.
- Li S., Li J., Chou I. Min, Jiang L. and Ding X. (2017a) The formation of the Yichun Ta-Nb deposit, South China, through fractional crystallization of magma indicated by fluid and silicate melt inclusions. *J. Asian. Earth. Sci.* **137**, 180–193.
- Li W., Kwon K. D., Li S. and Beard B. L. (2017b) Potassium isotope fractionation between K-salts and saturated aqueous solutions at room temperature: Laboratory experiments and theoretical calculations. *Geochim. Cosmochim. Acta* **214**, 1–13.
- Li X. and Liu Y. (2011) Equilibrium Se isotope equilibrium fractionation parameters: a first-principles study. *Earth Planet. Sci. Lett.* **304**, 113–120.
- Li Y., Wang W., Huang S., Wang K. and Wu Z. (2019) First-principles investigation of the concentration effect on equilibrium fractionation of K isotopes in feldspars. *Geochim. Cosmochim. Acta* **245**, 374–384.
- Livingston D. A. (1963) Chemical composition of Rivers and Lakes. In (M. Fleischered.,) Data of Geochemistry, sixth edition. Chapter G. USGS Prof. Paper 440-G. 64pp.
- Liu S., Li Y., Ju Y., Liu J., Liu J. and Shi Y. (2018) Equilibrium nickel isotope fractionation in nickel sulfide minerals. *Geochim. Cosmochim. Acta* **222**, 1–16.
- Lodders K. (2003) Solar system abundances and condensation temperatures of the elements. *Astrophys. J.* **591**, 1220–1247.
- Luo M. J., Liu C. L., Jiang Y. F., Xue J., Li P. and Yu J. G. (2009) Green recovery of potassium and aluminum elements from alunite tailings using gradient leaching process. *J. Clean. Prod.* **168**, 1080–1090.
- Mancinelli R., Botti A., Bruni F., Ricci M. A. and Soper A. K. (2007) Hydration of sodium, potassium, and chloride ions in



- solution and the concept of structure maker/breaker. *J. Phys. Chem. B* **111**, 13570–13577.
- Majzlan J., Speziale S., Duffy T. S. and Burns P. C. (2006) Single-crystal elastic properties of alunite,  $\text{KAl}_3(\text{SO}_4)_2(\text{OH})_6$ . *Phys. Chem. Miner.* **33**, 567–573.
- McKeown D. A., Bell M. I. and Etz E. S. (1999a) Raman spectra and vibrational analysis of the trioctahedral mica phlogopite. *Am. Mineral.* **84**, 970–976.
- McKeown D. A., Bell M. I. and Etz E. S. (1999b) Vibrational analysis of the dioctahedral mica: 2M1 muscovite. *Am. Mineral.* **84**, 1041–1048.
- Medhurst A. D., Rennie G., Chapman C. G., Meadows H., Duckworth M. D., Kelsell R. E., Gloger I. I. and Pangalos M. N. (2001) Distribution analysis of human two pore domain potassium channels in tissues of the central nervous system and periphery. *Brain Res. Mol. Brain Res.* **86**, 101–114.
- Méheut M. and Schauble E. A. (2014) Silicon isotope fractionation in silicate minerals: Insights from first-principles models of phyllosilicates, albite and pyrope. *Geochim. Cosmochim. Acta* **134**, 137–154.
- Méheut M., Lazzeri M., Balan E. and Mauri F. (2009) Structural control over equilibrium silicon and oxygen isotopic fractionation: a first-principles density-functional theory study. *Chem. Geol.* **258**, 28–37.
- Merlino S., Franco E., Mattia C. A., Pasero M. and de Gennaro M. (1985) The crystal structure of panunzite (natural tetrahedral silicate). *Neues Jahrbuch für Mineralogie, Monatshefte* **1985**, 322–328.
- Millero F. J., Feistel R., Wright D. G. and McDougall T. J. (2008) The composition of standard seawater and the definition of the reference-composition salinity scale. *Deep Sea Res. I* **55**(1), 50–72.
- Morgan L. E., Santiago Ramos D. P., Lloyd N. S. and Higgins J. A. (2018) High precision  $^{41}\text{K}/^{39}\text{K}$  measurements by MCICP-MS indicate terrestrial variability of  $\delta^{41}\text{K}$ . *J. Anal. Atom. Spectrom.* **33**, 175–186.
- Musić S., Živko-Babić J., Mehulić K., Ristić M., Popović S., Furić K., Selinger-Kocijan D., Čelap S. and Ivaniš T. (1997) Microstructural Properties of Leucite-type Glass-ceramics for Dental Use. *Croat. Chem. Acta* **70**, 703–718.
- Nimmo J. and Lucas B. (1973) A neutron diffraction determination of the crystal structure of alpha-phase potassium nitrate at 25 °C and 100 °C. *J. Phys. C: Solid State Phys.* **6**, 201–211.
- Nitta I., Tomiie Y. and Koo C. H. (1952) The crystal structure of potassium bicarbonate,  $\text{KHCO}_3$ . *Acta Crystallogr. A* **5**, 292–292.
- Parendo Christopher A., Jacobsen Stein B. and Wang Ku (2017) K isotopes as a tracer of seafloor hydrothermal alteration. *PNAS* **114**, 1827–1831.
- Perdew J. P. and Zunger A. (1981) Self-interaction correction to density-functional approximations for many-electron systems. *Phys. Rev. B* **23**, 5048–5079.
- Qian W., Wang W., Zou F. and Wu Z. (2018) Elasticity of orthoenstatite at high pressure and temperature: implications for the origin of low VP/VS zones in the mantle wedge. *Geophys. Res. Lett.* **45**(2), 665–673.
- Redhammer G. J. and Roth G. (2002) Single-crystal structure refinements and crystal chemistry of synthetic trioctahedral micas  $\text{KM}_3(\text{Al}^{3+}, \text{Si}^{4+})_4\text{O}_{10}(\text{OH})_2$ , where  $\text{M} = \text{Ni}^{2+}, \text{Mg}^{2+}, \text{Co}^{2+}, \text{Fe}^{2+}$ , or  $\text{Al}^{3+}$ . *Am. Mineral.* **87**, 1464–1476.
- Rowley C. N. and Roux B. (2012) The Solvation Structure of  $\text{Na}^+$  and  $\text{K}^+$  in Liquid Water Determined from High Level ab Initio Molecular Dynamics Simulations. *J. Chem. Theory Comput.* **8**, 3526–3535.
- Richardson S. M. and Richardson J. W. (1982) Crystal structure of a pink muscovite from Archer's Post, Kenya: implications for reverse pleochroism in dioctahedral micas. *Am. Mineral.* **67**, 69–75.
- Rudnick R. L. and Gao S. (2003) 3.01 - Composition of the Continental Crust. *Treatise Geochem.* **3**, 1–64.
- Rütter H. and Mootz D. (1991) Hydrate schwacher und starker Basen. V. Die Kristallstrukturen von  $\text{KOH} \cdot 2\text{H}_2\text{O}$  (Substruktur) und  $\text{KOH} \cdot 4\text{H}_2\text{O}$ . *Z. anorg. allg. Chem.* **601**, 73–82.
- Schauble E. A. (2011) First-principles estimates of equilibrium magnesium isotope equilibrium fractionation in silicate, oxide, carbonate and hexaaquamagnesium(2+) crystals. *Geochim. Cosmochim. Acta* **75**, 844–869.
- Schauble E., Rossman G. R. and Taylor H. P. (2004) Theoretical estimates of equilibrium chromium-isotope equilibrium fractionations. *Chem. Geol.* **205**, 99–114.
- Shannon R. D. (1976) Revised effective ionic radii and systematic studies of interatomic distances in halides and chalcogenides. *Acta Crystallogr. A* **32**, 751–767.
- Skakle J. M. S., Wilson M., Feldmann J. (2001) Dipotassium carbonate sesquihydrate: re-refinement against new intensity data. Acta Crystallographica Section E, Structure Reports Online. 57.
- Sueda Y., Irifune T., Nishiyama N., Rapp R. P., Ferroir T., Onozawa T., Yagi T., Merkel S., Miyajima N. and Funakoshi K. (2004) A new high-pressure form of  $\text{KAlSi}_3\text{O}_8$  under lower mantle conditions. *Geophys. Res. Lett.* **31**, L23612.
- Tian Z., Chen H., Fegley, Jr., B., Lodders K., Barrat J.-A. and Wang K. (2018) Potassium Isotope Differences among Chondrites, Earth, Moon, Mars, and 4-Vesta - Implication on the Planet Accretion Mechanisms. *Lunar Planet. Sci. Conf.* **49**, 1276.
- Urey H. C. (1947) The thermodynamic properties of isotopic substances. *J. Chem. Soc. (London)*, 562–581.
- Varma S. and Rempe S. B. (2006) Coordination numbers of alkali metal ions in aqueous solutions. *Biophys. Chem.* **124**, 192–199.
- Walker D., Verma P. K., Cranswick L. M. D., Jones R. L., Clark S. M. and Buhre S. (2004) Halite-sylvite thermoelasticity. *Am. Miner.* **89**, 204.
- Wang K. and Jacobsen S. B. (2016a) An estimate of the bulk silicate earth potassium isotopic composition based on MC-ICPMS measurements of basalts. *Geochim. Cosmochim. Acta* **178**, 223–232.
- Wang K. and Jacobsen S. B. (2016b) Potassium isotopic evidence for a high-energy giant impact origin of the Moon. *Nature* **538**, 487–490.
- Wang W., Qin T., Zhou C., Huang S., Wu Z. and Huang F. (2017a) Concentration effect on equilibrium fractionation of Mg-Ca isotopes in carbonate minerals: insights from first-principles calculations. *Geochim. Cosmochim. Acta* **208**, 185–197.
- Wang W., Zhou C., Qin T., Kang J., Huang S., Wu Z. and Huang F. (2017b) Effect of Ca content on equilibrium Ca isotope equilibrium fractionation between orthopyroxene and clinopyroxene. *Geochim. Cosmochim. Acta* **219**, 44–56.
- Wedepohl K. H. (1978) *Handbook of Geochemistry, Vol. III/2, Elements Si(14) to V(23)*. Springer-Verlag Press, Heidelberg.
- Wentzcovitch R. M. (1991) Invariant molecular-dynamics approach to structural phase transitions. *Phys. Rev. B* **44**, 2358–2361.
- Wu Z., Huang F. and Huang S. (2015) Isotope equilibrium fractionation induced by phase transformation: first-principles investigation for  $\text{Mg}_2\text{SiO}_4$ . *Earth Planet. Sci. Lett.* **409**, 339–347.
- Xu Y., Hu Y., Chen X., Huang T., Sletten R. S., Zhu D. and Teng F. (2019) Potassium isotopic compositions of international geological reference materials. *Chem. Geol.* **513**, 101–107.



- Yong W., Dachs E., Withers A. and Essene E. (2006) Heat capacity and phase equilibria of hollandite polymorph of  $\text{KAlSi}_3\text{O}_8$ . *Phys. Chem. Minerals*. **33**, 167–177.
- Young E. D., Tonui E., Manning C. E., Schauble E. and Macris C. A. (2009) Spinel-olivine magnesium isotope thermometry in the mantle and implications for the Mg isotopic composition of Earth. *Earth Planet. Sci. Lett.* **288**, 524–533.
- Zaccarini F., Thälhammer O. A. R., Princivalle F., Lenaz D., Stanley C. J. and Garuti G. (2007) Djerfisherite in the Guli dunite complex, polar Siberia: a primary or metasomatic phase?. *Can Mineral.* **45**, 1201–1221.
- Zhang J., Ko J. D., Hazen R. M. and Prewitt C. T. (1993) High-pressure crystal chemistry of  $\text{KAlSi}_3\text{O}_8$  hollandite. *Am. Mineral.* **78**, 493–499.

*Associate editor:* Edwin Schauble